

Resolving wave and laminar boundary layer scales for gap resonance problems

H. Wang^{1,†}, H. A. Wolgamot¹, S. Draper¹, W. Zhao¹, P. H. Taylor¹
and L. Cheng¹

¹Faculty of Engineering and Mathematical Sciences, The University of Western Australia,
35 Stirling Highway, Crawley, WA 6009, Australia

(Received 5 October 2018; revised 19 December 2018; accepted 1 February 2019;
first published online 18 March 2019)

Free surface oscillations in a narrow gap between elongated parallel bodies are studied numerically. As this represents both a highly resonant system and an arrangement of relevance to offshore operations, the nature of the damping is of primary interest, and has a critical role in determining the response. Previous experimental work has suggested that the damping could be attributed to laminar boundary layers; here our numerical wave tank successfully resolves both wave and boundary layer scales to provide strong numerical evidence in support of this conclusion. The simulations follow the experiments in using wave groups so that the computation is tractable, and both linear and second harmonic excitation of the gap are demonstrated.

Key words: wave–structure interactions

1. Introduction

Arranging ships or ship-shaped floating bodies in a closely spaced parallel alignment ('side-by-side') is necessary in some marine industrial applications, particularly transfer of liquefied natural gas from a floating production vessel to a carrier. This practice creates a long, narrow gap between the vessels, which supports highly resonant free surface motions at particular frequencies. As for any highly resonant system, the amplitude of the response depends on the system damping, and the resonance may be excited in a linear or nonlinear fashion. For industrial applications, the amplitude of the resonance during operations (moderate sea states) may be important in its own right, or due to its coupling with vessel motion.

It is well established that linear potential flow theory can predict resonant frequencies and mode shapes well (Molin 2001; Sun, Eatock Taylor & Taylor 2010; Molin *et al.* 2018). However, potential flow theory typically overpredicts experimentally determined resonant amplitudes of gap responses (e.g. Buchner, Van Dijk & De Wilde 2001) unless artificial dissipation is added (e.g. Chen 2005). Sources of this amplitude discrepancy are generally believed to be viscous effects and perhaps effects associated with the nonlinear free surface condition. The latter effect was investigated numerically by Feng & Bai (2015), who found only very

† Email address for correspondence: hongchao.wang2013@gmail.com

slight reductions in the amplitude of the resonant response even for rather steep incoming waves.

Thus, more effort has been focused on viscous dissipation. In an early experimental study of the gap problem, Molin *et al.* (2002) estimated the energy losses due to wall friction and flow separation at the (square) bilge for waves propagating in a long narrow channel; wall friction being approximately 15% of the total. Kristiansen & Faltinsen (2012) and Fredriksen, Kristiansen & Faltinsen (2015) created two-dimensional (2D) hybrid potential flow Navier–Stokes (NS) solver models to try to incorporate losses due to separation from the sharp bilges of catamaran boxes in forced heave and wave-excited heave and roll, and found good agreement with response curves from experiments. Faltinsen & Timokha (2015) and Tan *et al.* (2017) developed methods based on hydraulic arguments and calibration with 2D experimental data to modify potential flow solvers to correctly incorporate viscous losses.

Experimental studies have been crucial in the above work but largely focused on 2D geometries. Three-dimensional (3D) gap resonance experiments have been performed by Molin *et al.* (2009), Perić & Swan (2015) and Chua *et al.* (2018), amongst others. Recently Zhao *et al.* (2017) conducted 3D experiments in transient wave groups, for vessels with round and square bilges. In both cases substantial damping in addition to radiation damping was clearly present, and for the round bilge cases it was suggested that the damping was almost entirely due to laminar boundary layers.

NS solvers have been extensively applied to gap resonance in two dimensions, but less so in three, where the computational demand is greater. Feng *et al.* (2017) simulated regular waves interacting with the square bilge version of the 3D model tested by Molin *et al.* (2009), and found reasonable agreement with experimental response curves (generated from irregular wave tests). For each frequency considered, it was found necessary to run 20–50 wave periods, to ensure that steady state was reached. When the bilges were rounded, Feng *et al.* (2017) found that the response curves obtained from the NS solver agreed well with linear potential flow theory. A notable difference between this case and Zhao *et al.* (2017) was the gap width – the geometries being otherwise similar, the latter featured a gap width around half that of the former, which entails a large change in the relative contribution of viscous and radiation damping.

In this work two transient wave group experiments of Zhao *et al.* (2017) are reproduced using an NS solver – this ambitious effort enables comparison of time series rather than averaged responses, and by reducing the simulation time required (compared to using regular waves), increases the numerical resolution that can be used. By simulating one case with linear excitation and one case with frequency doubling, resolution of nonlinear free surface effects is demonstrated. The approach taken also enables a detailed investigation of the nature of the damping, to a resolution not feasible in experiments.

2. Re-creating experiments

In this section, experimental and numerical details of primary importance are presented; more complete information can be found in Zhao *et al.* (2017) and Wang *et al.* (2018), respectively.

2.1. Experimental

Zhao *et al.*'s (2017) experiments were carried out in the Deepwater Wave Basin at Shanghai Jiao Tong University. Two identical prismatic boxes of length $L = 3.333$ m,

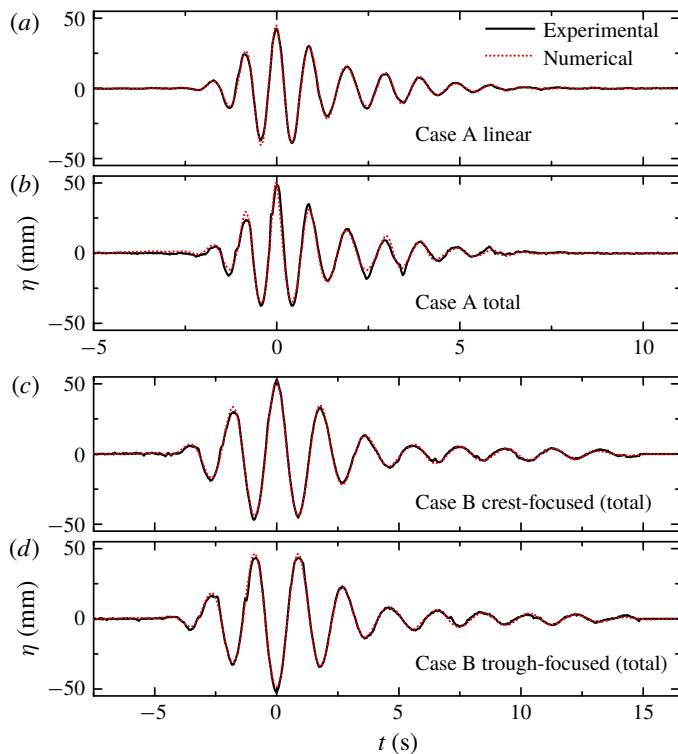


FIGURE 2. (Colour online) Comparison of numerical and experimental incident wave groups for cases A and B.

solved using a finite volume method discretised on a structured mesh. The origin of the NWT was positioned at the mean free surface at the centre of the gap, with x the direction of wave propagation and z positive upwards. The toolbox `waves2Foam` (Jacobsen, Fuhrman & Fredsøe 2012) was used for generation of incident waves and absorption of reflected waves using relaxation zones at both ends of the NWT. The experimental incident wave groups were re-created with considerable accuracy in the NWT using an iterative method (see figure 2 and Wang *et al.* (2018) for details). The size of the NWT must be minimised; the lengths of the NWT for cases A and B were chosen as $8.0\lambda_p$ and $5.2\lambda_p$, respectively, to allow wave propagation and absorption upstream and downstream of the boxes, while the water depths were λ_p and $0.58\lambda_p$ (which fulfil the deep-water condition). Sidewalls were set at $y=4L$ and $y=12L$ for cases A and B, respectively, to limit wave reflection.

Knowledge of Zhao *et al.*'s (2017) experiments informed the selection of mesh parameters shown in figure 1. The maximum Reynolds number here is $Re = \omega\eta_o^2/\nu \simeq 2.3 \times 10^4$, where ω is the first resonant frequency, ν the kinematic viscosity and η_o the amplitude of free surface motion at the centre of the gap, with a maximum value of around 0.06 m. For oscillatory flow over a smooth plane wall, turbulence first appears at $Re \simeq 10^5$ (Jensen, Sumer & Fredsøe 1989). However, the possibility of flow separation from the rounded bilge must also be considered. Here the maximum local Keulegan–Carpenter number $KC = 2\pi\eta_o/2r$ for flow around the rounded bilge is approximately 2.3. For flow around a cylinder Sumer & Fredsøe (2006) give flow regimes for a limited subset of $(KC-Re)$ space; for $Re \simeq 10^3$ there is no separation

for $KC < 1.1$. Given that the present geometry is not a cylinder, and the oscillatory flow is transient, the KC and Re regimes for this problem make it plausible that laminar boundary layers dominate the damping in this case, and the mesh design is based around this hypothesis. The thickness of a Stokes boundary layer based on the parameters above is around $\delta_{0.99} = 4.6\sqrt{2\nu/\omega} \simeq 2.5$ mm for the first mode. In light of this, four meshes A1–A4 with near-wall cell width normal to the box walls Δx_2 equal to 2.0, 0.4, 0.1 and 0.05 mm were used to simulate case A. The adjacent cells expand away from the wall to take account of the fact that the near-wall velocity gradient is much larger than that near the gap centre. The other mesh dimensions are essentially the same for the four cases. The mesh size along the wave propagation direction Δx_1 is chosen to achieve 200 cells per peak wavelength to resolve propagating incident waves. The vertical cell height Δz_1 is chosen to ensure the aspect ratio (i.e. $\Delta z_1/\Delta x_2$) remains small, so that 20 cells per wave height are used for mesh A1 while 50 cells per wave height are used for meshes A2–A4. Along the gap direction, the cell width in the gap (region 1 in figure 1(a), from the mid-ship position $y = 0$ to the gap end $y = -L/2$) is chosen to give 60 cells per ‘wavelength’ of the seventh mode shape. The cell width outside the gap (region 2 in figure 1(a), from the gap end to the sidewall) expands gradually away from the gap end. Given that attached laminar boundary layers are expected, a symmetry boundary condition was applied at the mid-ship plane (see figure 1a) to reduce the computational cost. However, due to the two-scale nature of this problem, in which surface wavelength and boundary layer scales are resolved simultaneously, the number of cells is still extremely large, which renders the 3D simulations very demanding (e.g. mesh A3 has 48.1 million cells and the simulation requires approximately 1 million CPU hours, computed using 720 cores on a Cray XC40 supercomputer with 2.6 GHz Intel Xeon E5-2690 v3 ‘Haswell’ CPUs). For robustness, the time step of the simulations was chosen to be runtime adaptive with maximum Courant number not exceeding 0.5 (chosen based on experience). Although the gap is relatively narrow, surface tension is not represented numerically, since the Bond number $B_o = gL^2\rho/T_s \simeq 1.5 \times 10^6$ (where g and ρ are gravitational acceleration and fluid density, respectively, and $T_s = 0.073$ N m⁻¹ is the surface tension). This is well above the range where surface tension is important, according to Faltinsen & Timokha (2009).

2.3. Kinematics: linear excitation

The same incident crest-focused wave group corresponding to case A has been used to excite gap motions for meshes A1–A4. The excitation resulting from this wave group is mostly linear because the frequency content of the wave group overlaps with the natural frequencies of the dominant gap modal responses. Based on the arguments above, the near-wall velocity profile should resemble a Stokes boundary layer for oscillatory flow over an infinite flat plate. Here, however, there are multiple oscillation frequencies, all associated with time-varying amplitude and the hull is finite and rounded (though $r \gg \delta_{0.99}$). To compare the boundary layer profile computed in the vertical part of the gap in the NWT to this theory, a velocity-based time-dependent pressure gradient is used to numerically solve the Stokes equation,

$$\Delta p(t) = -\rho \frac{\partial u}{\partial t} + \mu \frac{\partial^2 u}{\partial x^2} + \rho g, \quad (2.1)$$

where u represents vertical fluid velocity. To calculate the vertical velocity profile away from a point on the wall in the straight part of the gap, at a depth which the

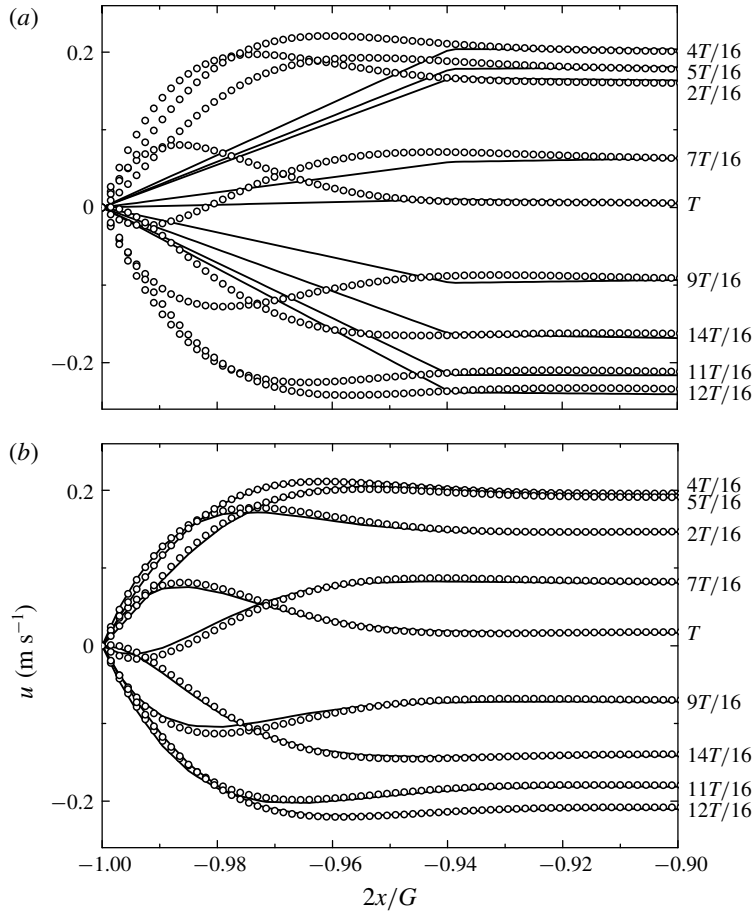


FIGURE 3. Boundary layer profiles in the gap at various phases over a nominal cycle T (from 8.12 s to 9.10 s) computed numerically (thin lines) and using (2.1) (circles) for meshes (a) A1 and (b) A3, at $y=0$, $z=-0.43D$.

free surface does not reach, the velocity-based pressure gradient $\Delta p(t)$ taken from the full 3D simulation at $0.05G$ away from the wall is applied in (2.1) (this sampling point is close to the wall but still outside the boundary layer). Agreement between the theoretical solution and the 3D simulation results becomes better as the near-wall mesh is refined, such that A3 and A4 give excellent agreement; the results of A1 and A3 for the point $(-G/2, 0, -0.43D)$ based on $\Delta p(t)$ from $(-0.9G/2, 0, -0.43D)$ are shown in figure 3. Similar results apply for other points.

Time series of free surface elevation at the centre of the gap for meshes A1–A4 are compared in figure 4(a). The phases from meshes A2, A3 and A4 agree well, while A1 leads the other three slightly. In terms of amplitude, the gap responses decay more swiftly as the near-wall mesh is refined. It is clear that, after the initial ‘excitation’ stage the responses of $A1 > A2 > A3 \simeq A4$. Based on figures 3 and 4(a), we conclude that convergence is achieved for mesh A3. Thus, in figure 4(b) the responses at the centre of the gap computed using A3 are compared to the experimental measurements of Zhao *et al.* (2017). The agreement between the simulations and experiments is good. The slight overpredictions which occur periodically arise because multiple

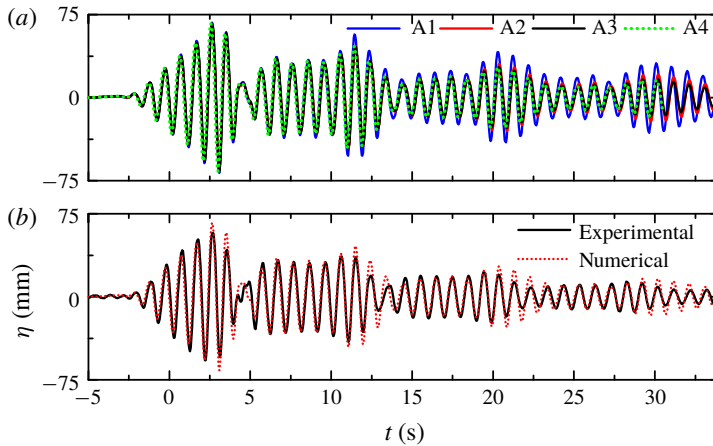


FIGURE 4. (Colour online) Response at gap centre for meshes A1–A4 (a) and that from mesh A3 compared to Zhao’s experiments (b) for case A (linear excitation). The time axes are as in figure 2.

modes are excited (see § 3.1), each with small errors in amplitude and phase (due to the numerical incident waves, experimental set-up, etc.). Such errors are noticeable at times in the response when multiple modes reinforce or cancel.

The full interaction of the wave group with the boxes is shown in supplementary movie 1 (available at <https://doi.org/10.1017/jfm.2019.115>). Snapshots of the interaction at $t=0$ and 1.8 s are shown in figure 5. The large wave crest is essentially unaltered at the edge of the figure (downstream and outside the boxes), whereas waves are almost absent downstream and behind the boxes in region 1 (see figure 1). This illustrates the strongly directional nature of the waves scattered from the boxes – most energy is reflected back up-wave and a small amount excites free surface modes within the gap. The ‘near-trapped’ wave energy then causes the fluid in the gap to oscillate within the side-by-side system, slowly leaking wave energy out into the external wave field. As a result, the gap oscillations persist long after the incident group has passed, as shown in supplementary movie 1. Higher-frequency scattered waves are also evident radiating from the gap in figure 5(b), and upstream of the leading box.

2.4. Kinematics: nonlinear excitation

Meshes B1 and B3, identical to A1 and A3 in the gap region, were used to compute responses to two wave groups for case B, shown in figure 2 and labelled crest-focused and trough-focused (in which each frequency component in the linear spectrum of the crest-focused wave is phase-shifted by 180°). For these wave groups the gap modes are excited nonlinearly through quadratic wave–wave–structure interactions. As in the experiments, the two-phase runs allowed odd and even harmonics to be extracted using the phase inversion method of Fitzgerald *et al.* (2014), with the results presented in figure 6 for mesh B3. There are some discrepancies between the numerical and experimental results for the (very small) long-wave difference component when $t < 1.6$ s but the agreement is better from $t = 1.6$ s onwards. The numerical and experimental first-, second- and third-order harmonics are in good agreement. As for case A, periodically the agreement deteriorates; seen in this light

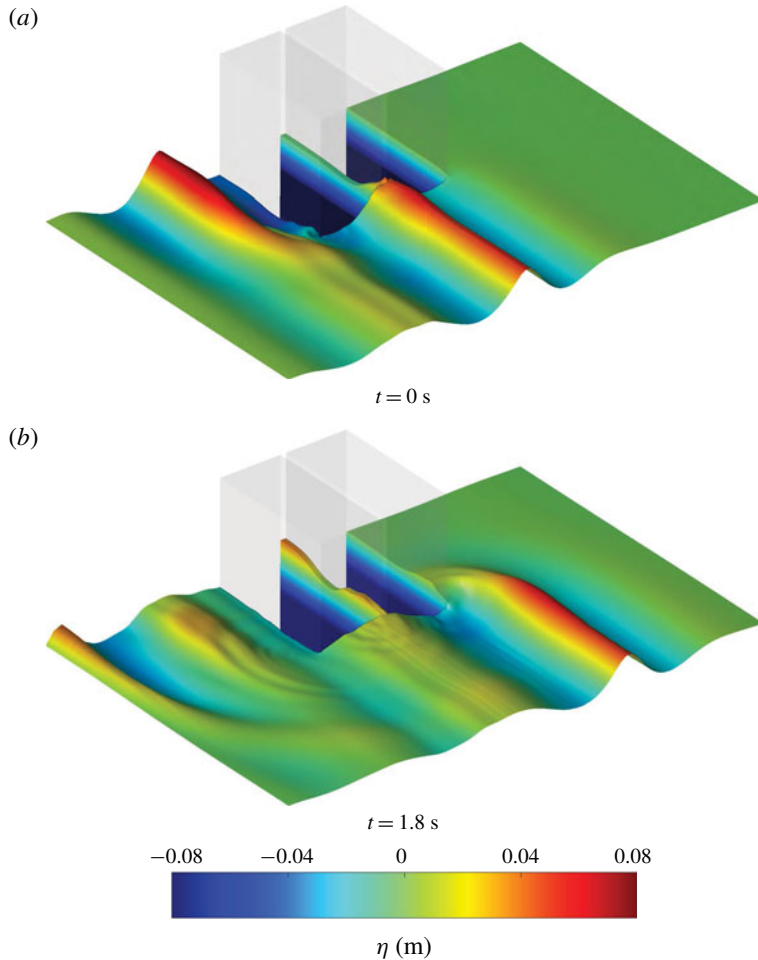


FIGURE 5. (Colour online) Snapshots of numerically computed response wave field for mesh A3 (in the region $2.5 \text{ m} < x < 8.5 \text{ m}$, $-4.0 \text{ m} < y < 0 \text{ m}$) captured at different times. Note that the vertical axis is stretched, such that 1 unit in the vertical equals 5 units in the horizontal, to more clearly show the free surface motions. To this end, the boxes are shown as transparent.

the third harmonic result is remarkable. The agreement for the fourth harmonic is not as good as for the other harmonics. However, assuming there is a generalised Stokes-type perturbation expansion for the gap responses, it is possible to match the envelope of the fourth harmonic component by squaring the envelope of the second harmonic (calculated as $\sqrt{\eta_2^2 + \eta_{2H}^2}$, where η_{2H} is the Hilbert transform of the second harmonic free surface elevation η_2) and then fitting the measured envelope of the fourth harmonic component by a least-squares method. Figure 6(h) shows that the extracted fourth harmonic fits the scaled squared envelopes of the second harmonic quite well, demonstrating that the numerical results are self-consistent. These results represent a highly successful application of an NS solver to a problem with linear viscous dissipation but nonlinear free surface effects, both of which must be resolved to achieve satisfactory results. NS solvers have previously been used to derive second harmonic responses around non-resonant structures such as cylinders in relatively

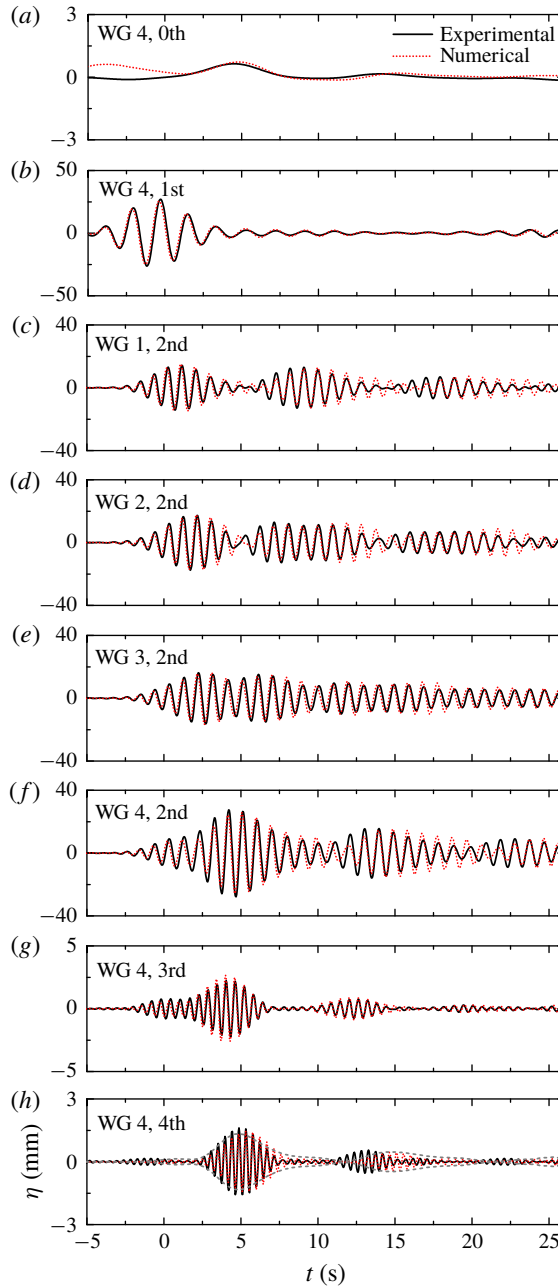


FIGURE 6. (Colour online) Comparison of experimentally and numerically (mesh B3) determined harmonic responses: (a) long-wave difference component; (b) first harmonic; (c–f) second harmonic; (g) third harmonic; and (h) fourth harmonic, with scaled envelope squared of the second harmonic (dashed grey lines). The time axes are as in figure 2.

steep waves (Paulsen *et al.* 2014). Here the strength of the second harmonic response is much stronger; even in waves which are not very steep, the second harmonic responses are as large as the first.

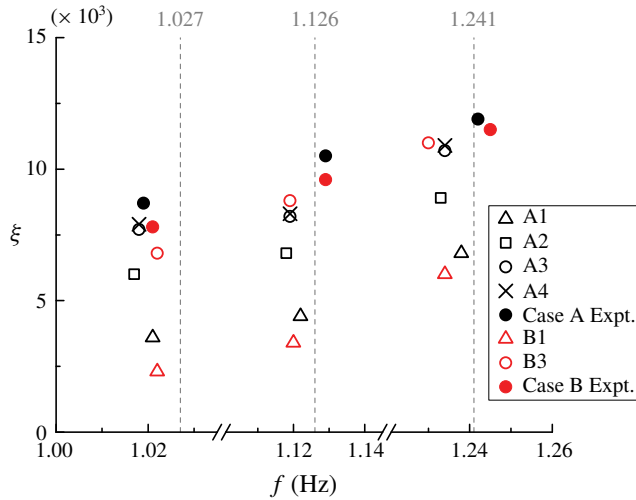


FIGURE 7. (Colour online) Non-dimensional damping coefficient for each mode versus frequency (discontinuous axis) for each numerical simulation compared to experimental results. The modes shown are modes 1, 3 and 5 (from left to right). The grey dashed vertical lines and values above represent the resonant frequencies obtained from the potential flow software DIFFRACT.

3. Damping analysis

3.1. Global damping

Owing to the transient nature of the incident wave group, the gap response can be conceptualised as occurring in two stages, i.e. the excitation stage when the incident waves drive the gap motions, and the decay stage, when the incident waves have passed and the gap motion is a pure oscillatory decay. If the total damping in this decay stage is linear, the free surface elevations should be well represented by a series of decaying sinusoids with frequencies corresponding to the gap modes, as in Zhao *et al.* (2017). Thus

$$\eta(t) = \sum_n A_n \sin(\omega_n t + \phi_n) \exp[-\omega_n \xi_n t], \quad (3.1)$$

where $f_n = \omega_n/2\pi$ is the resonant frequency of the n th mode, ξ_n the normalised modal damping, and A_n and ϕ_n the amplitude and phase at the start of the time window. The method of Kumaresan & Tufts (1982) performs well in estimating the parameters of exponentially damped sinusoids for short data records, and is used here to calculate the modal parameters using free surface elevation time series at a number of points in the gap, assuming f_n and ξ_n are independent of position along the gap, while A_n and ϕ_n vary with position (reflecting the modal spatial structure). The effectiveness of applying this method to the gap resonance problem has been demonstrated in Zhao *et al.* (2017). Choosing a 20 s time window of $t = [9, 29]$ s, the analysis is conducted for the experimental and numerical results for cases A and B. The resonant frequencies and corresponding damping coefficients are shown in figure 7.

Figure 7 suggests that the first resonant frequency identified from the numerical results matches the experimental value more closely than potential flow theory for the

first mode, while the opposite is true for the higher modes. Nevertheless, the frequency agreement in all cases is quite good (within 1%). The modal damping values are of primary interest, and approach the experimental levels from below as the mesh is gradually refined and the boundary layer resolved. For the finer meshes A3 and A4 the damping is in satisfactory agreement with the experimental values, despite being slightly smaller. Part of this error may be attributable to the temperature dependence of viscosity – in the simulations $\mu = 1000 \mu\text{Pa s}$, while temperatures in the Shanghai basin during the tests were 17°C , giving $\mu = 1080 \mu\text{Pa s}$. Damping values for each mode are similar for cases A and B, while the third mode is generally underpredicted more than the others.

From the numerical point of view, a coarse mesh usually induces larger unphysical diffusion than a finer mesh, so it is common for fluid damping to be overpredicted when mesh refinement is inadequate. Here, however, it appears that the damping induced by wall friction dominates any unphysical diffusion. In this case the diffusion should be small, since the structured mesh in the gap follows the curvature of the walls and the convection term is small since the gap flow is Stokes-like. At this point, note should be made of the work of Kristiansen & Faltinsen (2012), who demonstrated convergence of gap responses by varying the number of uniform cells across the gap and concluded that gap responses were not sensitive to mesh refinement in the gap for their 2D geometry with square bilges. However, for the geometry with rounded bilges in the present study, it is emphasised that the gap responses can only be predicted with good accuracy when the boundary layer scale is resolved properly.

3.2. Local damping

While the ‘global’ damping of the computed free surface motions appears satisfactory, the advantage of numerical simulations is that the flow field can be interrogated in detail. It is of interest to determine whether the local fluid behaviour supports the supposition that the viscous damping is due to laminar boundary layers. Contours of normalised vorticity have been computed and examined, though they are not shown here, as no visible vortex shedding occurs from the bilges throughout the simulation, while small vortex shedding occurs from the sharp corners at the gap ends during the excitation phase. To more quantitatively assess the nature of the dissipation, the viscous dissipation is computed for various control volumes. The rate of energy dissipation by the action of viscosity per unit time in a control volume V can be calculated as (Whitham 1963)

$$\dot{E}_v = \frac{1}{2} \int_V \mu (e_{xx}^2 + e_{yy}^2 + e_{zz}^2 + 2e_{yz}^2 + 2e_{zx}^2 + 2e_{xy}^2) dV, \quad (3.2)$$

where $e_{xx} = 2(\partial u_x/\partial x)$, $e_{xy} = \partial u_y/\partial x + \partial u_x/\partial y$, etc. are the rate-of-strain components. To attempt to separate the possible viscous dissipation contributions from wall friction and flow separation, two control volumes are used. Control volume V_1 surrounds the boxes with x bounds $[-1.25, 1.25] \times (G/2 + B)$, z extending from the NWT floor to the time-varying free surface η and y out to $0.56L$. Control volume V_2 is a thin layer surrounding the boxes with a thickness $\delta = 3 \text{ mm}$ (the blue area in cross-section shown in figure 8 projecting along the gap). The viscous dissipation rates in these control volumes are compared in figure 8. It is found that the largest difference between V_1 and V_2 at any time in the decay stage is less than 8%, and the cumulative difference in viscous dissipation (integrating over time from $t = 9 \text{ s}$ to $t = 29 \text{ s}$) is less than 2%, which means that nearly all of the viscous dissipation

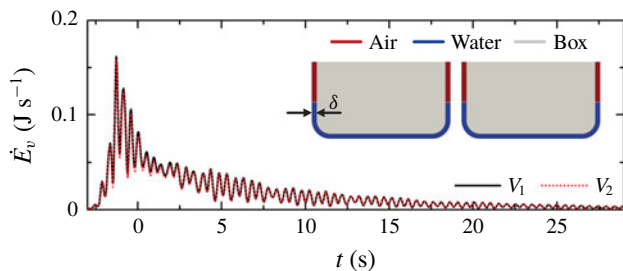


FIGURE 8. (Colour online) Dissipation rate time series for control volumes V_1 and V_2 , mesh A3, case A and (inset) cross-section diagram of control volume V_2 , for which $\delta = 3$ mm.

occurs in a thin layer surrounding the boxes, suggesting that laminar boundary layers are indeed the dominant damping contribution.

Having computed the viscous dissipation rate, it is possible to use this to compute (at least approximately) the expected decay rate of the free surface in the gap and compare to that found in the simulation, on a modal basis. It is therefore necessary to obtain estimates of the average rate of energy loss from the oscillating system (\dot{E}_n) and the amount of energy stored in the oscillating system (E_n) for each mode (per unit modal amplitude squared), which are related to the non-dimensional damping for each mode by

$$\xi_n \propto \frac{\dot{E}_n}{E_n}, \quad (3.3)$$

(when the damping is small) assuming that the gap decay is well described by (3.1). The total rate of energy loss is assumed to be the sum of radiation and viscous contributions, i.e. $\dot{E}_n = \dot{E}_r^n + \dot{E}_v^n$. As the total energy of the oscillating system E_n should be the same for viscous or inviscid calculations, we can write

$$\xi_n = \dot{E}_n \times \frac{\xi_r^n}{\dot{E}_r^n}, \quad (3.4)$$

where ξ_r^n and \dot{E}_r^n are the damping coefficient and rate of dissipation, respectively, caused by radiation by mode n . These have been calculated using the linear potential flow software DIFFRACT, which is convenient as the different modal contributions are computed separately. The radiated wave field is obtained by subtracting the scattered wave field from a large box of width $(2B + G)$ from the scattered field for the gap problem. This approach takes advantage of the narrowness of the gap, and is evidently deficient close to the ends of the gap, but otherwise produces smooth, symmetrical radiated wave fields. For each mode, the rate of energy radiation to infinity is computed using the radiated field at large radius from the boxes – radiation patterns are shown in figure 9. It is interesting that mode 1 radiates most strongly perpendicular to the gap (or along the NWT) while the other modes radiate most strongly around the direction along the gap (i.e. out the ends of the gap).

To complete the analysis, the viscous dissipation rates shown in figure 8 must be separated into modal contributions. Given the form of (3.2) and that the velocity in the gap is in a form similar to (3.1), with spatial decay of the velocity towards the wall, it is clear that for each mode there are dissipation rate contributions which are

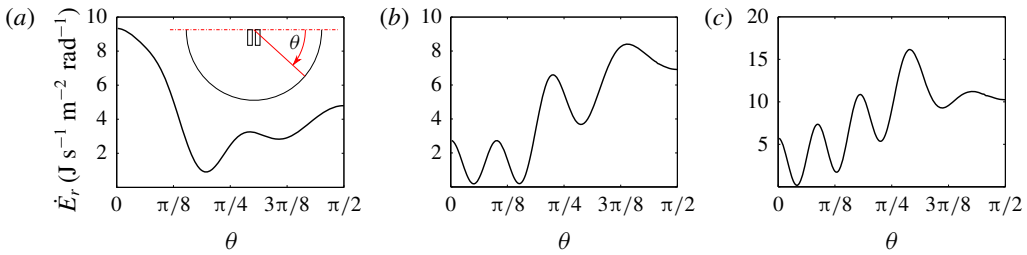


FIGURE 9. (Colour online) Radiation pattern, in terms of energy loss per unit modal amplitude squared per radian, from gap mode 1 (*a*), mode 3 (*b*) and mode 5 (*c*) determined using linear potential flow software DIFFRACT in an unbounded domain. The definition sketch of θ is shown in (*a*) and $\theta = \pi/2$ is along the gap direction.

purely decaying in time, and those which oscillate at twice the gap mode frequencies. In addition, there are sum and difference frequency terms (cross-mode terms) and terms at the gap oscillation frequencies caused by the time dependence of V in (3.2) (due to the varying run-up on the box). Were the oscillations constant-amplitude instead of decaying, time-integrating the dissipation rate to recover the average or total dissipation would remove all of the oscillatory terms, leaving only the mean. In this case we say simply that we expect the pure decay terms to dominate. As the double-frequency dissipation rate terms occur in the same proportion as the pure decay terms, it is possible to fit the double-frequency terms using the same method as applied above (after isolating them with a bandpass filter), and use the relative amplitudes to divide the pure decay dissipation rate signal into modal contributions. Once the modal components of viscous dissipation rate are obtained, the global damping coefficients for each mode can be calculated according to (3.4).

The analysis described above is carried out on the viscous dissipation rate time series from $t_0 = 9$ s onwards for mesh A3. The amplitude spectrum of the viscous dissipation rate is obtained using the fast Fourier transform as shown in figure 10(*a*), while the high-pass and low-pass time series are shown in figure 10(*b*). Applying the method of Kumaresan & Tufts (1982) to the high-pass signal, it is found that the reconstructed signal gives a very good approximation of the original high-pass signal (see figure 11(*a*)). The modal frequencies ω_{vh}^n and non-dimensional ‘damping’ ξ_{vh}^n determined from the double-frequency viscous dissipation rate terms closely match those for the free surface elevations over the same period (within 0.1 % for frequencies and 3 % for damping), which means the coupling between different modes is indeed weak as expected. The low-pass viscous dissipation rate signal should contain modal signals with the same modal rates of decay and proportionality coefficients

$$\alpha_n = \frac{\dot{E}_{vh}^n(t_0)}{\dot{E}_{vh}(t_0)} \quad (3.5)$$

as the high-pass signal. Thus, the dominant term in the low-pass signal can be expressed as the sum of three pure decay curves ($n = 1, 3, 5$) in the appropriate ratio (α_n) and scaled by a constant C as

$$\dot{E}_v = \sum_n C \alpha_n \exp[-2\omega_{vh}^n \xi_{vh}^n t]. \quad (3.6)$$

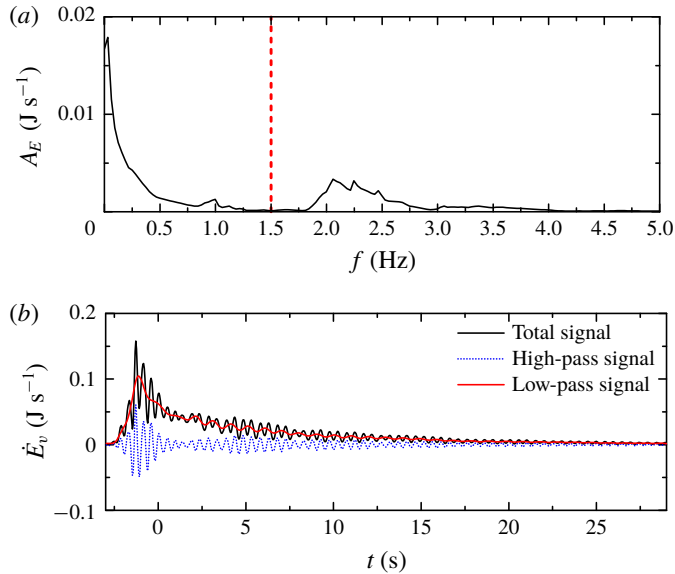


FIGURE 10. (Colour online) Amplitude spectrum (a), and high-pass and low-pass time series (b) of viscous dissipation rate from $t = -3$ to $t = 29$ s. In (a), double-frequency peaks corresponding to the three main gap modes can clearly be seen between 2 and 2.5 Hz, and the red dashed line represents the cut-off frequency for the filters.

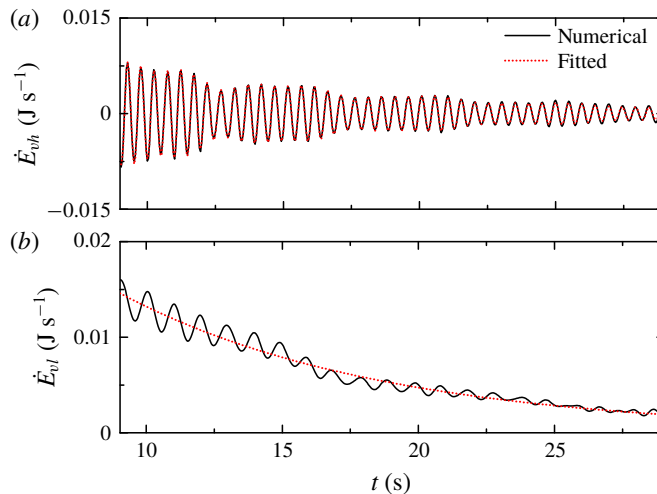


FIGURE 11. (Colour online) Numerical fit of high-pass (a) and low-pass (b) viscous dissipation rate time series, using the method of Kumaresan & Tufts (1982) and a least-squares method, respectively.

A numerical fit based on a least-squares method gives very good agreement with the original signal shown in figure 11(b), with the coefficient of determination $R^2 = 0.96$, meaning that \dot{E}_v^n has been determined.

	Mode 1	Mode 3	Mode 5
ξ_η	7.7	8.3	11.2
ξ_μ	6.6	9.1	9.5

TABLE 1. Values of $\xi \times 10^3$ determined from ‘global’ η (corresponding to the damping coefficients in figure 7) and ‘local’ μ analyses.

Using (3.4) we arrive at the global damping results shown in table 1, where ξ_η is the global damping derived from the free surface elevations and shown in figure 7 and ξ_μ is the global damping derived using the dissipation calculation. The comparison is reasonable (in light of the caveats discussed below), confirming the consistency of these results, and the conclusion that the viscous damping is dominated by laminar boundary layer behaviour.

It should be emphasised that producing a global damping value from radiation and viscous contributions in the manner undertaken here involves several approximations, some mentioned above, and some discussed here. Using (3.1) to represent the gap motions works well because each mode may be described by a complex resonance (see e.g. Meylan & Eatock Taylor 2009), though using the radiation damping behaviour from a single (real) frequency is not a rigorous application of this theory; ideally complex frequency calculations would be used. Secondly, the radiation behaviour in the NWT and potential flow are assumed to be the same. As the sidewalls of the NWT are reflective boundaries (while the ends are absorbing), this would tend to reduce the effective radiation damping compared to an unbounded domain potential flow analysis. However, numerical tests with a domain of larger width for mesh A1 did not yield larger damping values. In this case it is important to consider numerical propagation of the radiated wave, which is more than an order of magnitude smaller in amplitude than the gap oscillation or incident wave. As the vertical mesh resolution is optimised for propagation of the incident wave, it may be inadequate to correctly capture propagation of the radiated wave. This difference in scales therefore means that (unphysical) numerical damping of the wave radiated out of the gap reduces the effect of the reflective walls. The effect of the walls is therefore considered minor.

4. Conclusions

In this work numerical solutions of the Navier–Stokes equations have been shown to compare favourably with experimentally observed gap response time series, including higher harmonics, for (we believe) the first time. This is also an excellent test of the possibility of resolving wave and (laminar) boundary layer scale processes in the same simulation, as the amplitude of the resonant response for a narrow gap depends critically on the viscous dissipation, the nature of which cannot feasibly be determined in wave basin tests. Interrogation of the flow field has found that nearly all the viscous dissipation is confined to a thin layer surrounding the boxes, meaning the contribution from flow separation is negligible and wall friction is the main source of damping. Further, the viscous dissipation in the boundary layer has been computed, separated into modes and added to the modal radiation damping contribution to produce modal global damping coefficients in reasonable agreement with those measured in the simulation at the free surface, which are themselves in fairly good agreement with the experimental values.

In contrast to the finding of Kristiansen & Faltinsen (2012) that the 2D gap response with square bilges is not sensitive to the mesh in the gap, it has been shown that the cell width normal to the wall in the gap is crucial in determining the amplitude response of each of the gap modes for the 3D gap resonance problem with round bilges at laboratory scale. With a sufficiently fine mesh, the numerical near-wall boundary layer can be well predicted by solving a local Stokes equation driven by the time-varying pressure taken at a position near the wall in the gap but still outside the boundary layer.

Given the success of reproducing higher harmonics using the NS solver, it is expected that even higher harmonics could be well predicted if the mesh resolution near the free surface is further refined, though their practical significance may be limited. However, quadratic excitation of gap resonance does appear to be a problem of practical relevance.

Ultimately the gap resonance problem has industrial relevance at a substantially larger scale, though model testing remains a crucial tool for the offshore industry and it is vital to understand these tests. As the scale is increased, the boundary layers will inevitably become turbulent; though this is beyond the scale at which laboratory testing is feasible. For sharp corners or bilge keels, separation will occur in the laboratory as well as in the field.

Acknowledgements

This work was supported by the ARC Industrial Transformation Research Hub for Offshore Floating Facilities which is funded by the Australian Research Council, Woodside Energy, Shell, Bureau Veritas and Lloyds Register (grant no. IH140100012). The support in resources provided by the Pawsey Supercomputing Centre with funding from the Australian Government and the Government of Western Australia is acknowledged. The first author acknowledges support from IPRS, APA and Shell–UWA scholarships.

Supplementary movie

Supplementary movie is available at <https://doi.org/10.1017/jfm.2019.115>.

REFERENCES

- BUCHNER, B., VAN DIJK, A. & DE WILDE, J. 2001 Numerical multiple-body simulations of side-by-side mooring to an FPSO. In *The 11th Intl Offshore Polar Engng Conf.*, ISOPE.
- CHEN, X. B. 2005 Hydrodynamic analysis for offshore LNG terminals. In *Proceedings of the 2nd International Workshop on Applied Offshore Hydrodynamics, Rio de Janeiro*.
- CHUA, K. H., DE MELLO, P., MALTA, E., VIEIRA, D., WATAI, R., RUGGERI, F., EATOCK TAYLOR, R., NISHIMOTO, K. & CHOO, Y. S. 2018 Irregular seas model experiments on side-by-side barges. In *The 28th Intl Offshore Polar Engng Conf.*, ISOPE.
- FALTINSEN, O. M. & TIMOKHA, A. N. 2009 *Sloshing*. Cambridge University Press.
- FALTINSEN, O. M. & TIMOKHA, A. N. 2015 On damping of two-dimensional piston-mode sloshing in a rectangular moonpool under forced heave motions. *J. Fluid Mech.* **772**, R1.
- FENG, X. & BAI, W. 2015 Wave resonances in a narrow gap between two barges using fully nonlinear numerical simulation. *Appl. Ocean Res.* **50**, 119–129.
- FENG, X., BAI, W., CHEN, X. B., QIAN, L. & MA, Z. H. 2017 Numerical investigation of viscous effects on the gap resonance between side-by-side barges. *Ocean Engng* **145**, 44–58.

- FITZGERALD, C. J., TAYLOR, P. H., EATOCK TAYLOR, R., GRICE, J. & ZANG, J. 2014 Phase manipulation and the harmonic components of ringing forces on a surface-piercing column. *Proc. R. Soc. Lond. A* **470** (2168), 20130847.
- FREDRIKSEN, A. G., KRISTIENSEN, T. & FALTINSEN, O. M. 2015 Wave-induced response of a floating two-dimensional body with a moonpool. *Phil. Trans. R. Soc. Lond. A* **373** (2033), 20140109.
- JACOBSEN, N. G., FUHRMAN, D. R. & FREDSSØE, J. 2012 A wave generation toolbox for the open-source CFD library: OpenFoam[®]. *Intl J. Numer. Meth. Fluids* **70** (9), 1073–1088.
- JENSEN, B. L., SUMER, B. M. & FREDSSØE, J. 1989 Turbulent oscillatory boundary layers at high Reynolds numbers. *J. Fluid Mech.* **206**, 265–297.
- KRISTIENSEN, T. & FALTINSEN, O. M. 2012 Gap resonance analyzed by a new domain-decomposition method combining potential and viscous flow draft. *Appl. Ocean Res.* **34**, 198–208.
- KUMARESAN, R. & TUFTS, D. W. 1982 Estimating the parameters of exponentially damped sinusoids and pole-zero modeling in noise. *IEEE Trans. Acoust. Speech Signal Process.* **30** (6), 833–840.
- MEYLAN, M. H. & EATOCK TAYLOR, R. 2009 Time-dependent water-wave scattering by arrays of cylinders and the approximation of near trapping. *J. Fluid Mech.* **631**, 103–125.
- MOLIN, B. 2001 On the piston and sloshing modes in moonpools. *J. Fluid Mech.* **430**, 27–50.
- MOLIN, B., REMY, F., CAMHI, A. & LEDOUX, A. 2009 Experimental and numerical study of the gap resonances in-between two rectangular barges. In *13th Congress of the International Maritime Association of the Mediterranean, Istanbul, Turkey*. IMAM.
- MOLIN, B., REMY, F., KIMMOUN, O. & STASSEN, Y. 2002 Experimental study of the wave propagation and decay in a channel through a rigid ice-sheet. *Appl. Ocean Res.* **24** (5), 247–260.
- MOLIN, B., ZHANG, X., HUANG, H. & REMY, F. 2018 On natural modes in moonpools and gaps in finite depth. *J. Fluid Mech.* **840**, 530–554.
- PAULSEN, B. T., BREDMOSE, H., BINGHAM, H. B. & JACOBSEN, N. G. 2014 Forcing of a bottom-mounted circular cylinder by steep regular water waves at finite depth. *J. Fluid Mech.* **755**, 1–34.
- PERIĆ, M. & SWAN, C. 2015 An experimental study of the wave excitation in the gap between two closely spaced bodies, with implications for LNG offloading. *Appl. Ocean Res.* **51**, 320–330.
- SUMER, B. M. & FREDSSØE, J. 2006 *Hydrodynamics Around Cylindrical Structures*. World Scientific.
- SUN, L., EATOCK TAYLOR, R. & TAYLOR, P. H. 2010 First- and second-order analysis of resonant waves between adjacent barges. *J. Fluids Struct.* **26** (6), 954–978.
- TAN, L., LU, L., TANG, G. Q., CHENG, L. & CHEN, X. B. 2017 An energy dissipation model for wave resonance problems in narrow gaps formed by floating structures. In *32nd Intl Workshop on Water Waves and Floating Bodies, Dalian, China*.
- WANG, H., DRAPER, S., ZHAO, W., WOLGAMOT, H. A. & CHENG, L. 2018 Development of a computational fluid dynamics model to simulate three-dimensional gap resonance driven by surface waves. *J. Offshore Mech. Arctic Engng* **140** (6), 061803.
- WHITHAM, G. B. 1963 The Navier–Stokes equations of motion. In *Laminar Boundary Layers* (ed. L. Rosenhead). Clarendon Press.
- ZHAO, W., WOLGAMOT, H. A., TAYLOR, P. H. & EATOCK TAYLOR, R. 2017 Gap resonance and higher harmonics driven by focused transient wave groups. *J. Fluid Mech.* **812**, 905–939.